Buck and colleagues assess published reports suggesting that, in addition to its utility in staging and restaging lung cancer, ^{18}F-FDG PET provides significant prognostic information on patients with non–small cell lung cancer. . ***Page 1274***

Scheffel and Pomper look at the promise and potential limitations of current tracers used in PET imaging of gastrin-releasing peptide receptor expression in prostate cancer. . . . . ***Page 1277***

Lemke and colleagues report on incremental diagnostic information provided by retrospective PET/CT image fusion on data from patients with suspected pancreatic lesions. . . . . ***Page 1279***

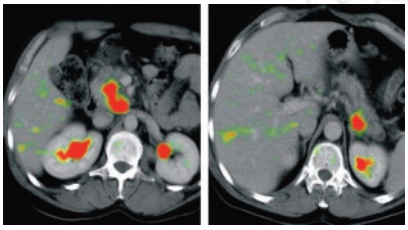

Erdi and colleagues evaluate the effects of motion and respiratory phase on standardized uptake values in PET/CT of patients with lung cancer. . . . . ***Page 1287***

Pirotte and colleagues compare the merits of ^{18}F-FDG and ^{11}C-methionine as tracers for PET-guided neurosurgical procedures on gliomas. . . . . ***Page 1293***

Knappen and colleagues investigate the advantages of the perfusable tissue index in noninvasive assessment of myocardial fibrosis in patients with idiopathic dilated cardiomyopathy. . . . . ***Page 1299***

Tanabe and colleagues apply ^{123}I-MIBG myocardial scintigraphy to the physiologic assessment of patients with panic disorder and find evidence of impaired cardiac sympathetic function. . . . . ***Page 1305***

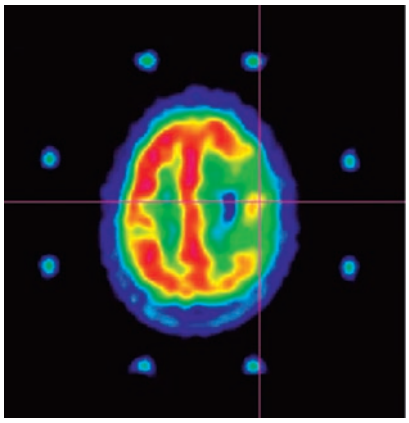

Wells and colleagues present results evaluating the utility of dSPECT, an iterative algorithm, in removing bladder artifacts from clinically acquired pelvic bone SPECT images. . . . . ***Page 1309***

Jani and colleagues assess the role of radioimmunoscintigraphy directed against prostate-specific membrane antigen in influencing radiotherapy toxicity and biochemical control after prostatectomy. . . . . ***Page 1315***

Fuster and colleagues compare the accuracy of ^{18}F-FDG PET with that of standard diagnostic clinical procedures in detecting locoregional disease and distant metastases in patients referred for suspected recurrent melanoma. . ***Page 1323***

Sundaram and colleagues describe a simplified kinetic analysis method for dynamic assessment of ^{18}F-FDG uptake in tumor. . . . . ***Page 1328***

Guo and colleagues investigate correlations between ^{18}F-FDG uptake in PET imaging, lactate and choline concentrations measured by in vitro ^{1}H magnetic resonance spectroscopy, and survival in human lung adenocarcinoma. . . . . ***Page 1334***

Bagheri and colleagues describe the additional value of ^{18}F-FDG PET/CT over PET alone in reliable visualization of the normal adrenal gland. . . . . ***Page 1340***

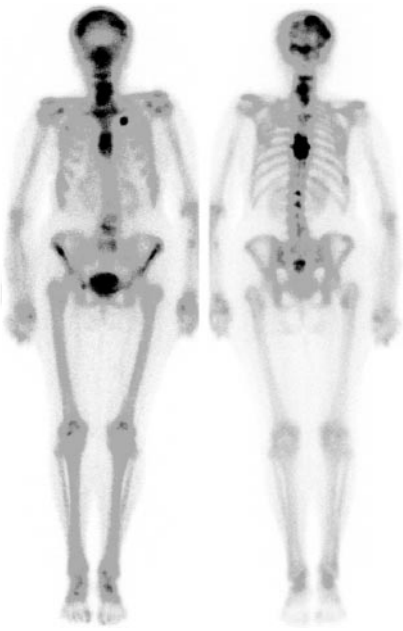

Weber and colleagues evaluate a continuous-infusion $H_2^{15}O$ PET and acetazolamide challenge protocol as an alternative to single-bolus injection for assessment of cerebral perfusion status in patients with cerebrovascular disease. . . . . ***Page 1344***

Oturai and colleagues compare the diagnostic accuracies of γ-camera PET and dedicated PET in patients with suspected lung cancer. . . . . ***Page 1351***

Pandit-Taskar and colleagues provide a comprehensive review of radiopharmaceuticals currently used for palliation in patients with osseous metastases, includ-

ing approved dosages, methods of administration, indications for use, and recommended guidelines. . . . . ***Page 1358***

Sgouros and colleagues describe and evaluate ^{124}I PET–based, patient-specific, 3-dimensional dosimetry for ^{131}I therapy in thyroid cancer. . . . . ***Page 1366***

Blankenberg and colleagues propose a novel imaging complex with a radiolabeled adapter protein bound to a docking tag and fused to a targeting protein as a model system for targeted imaging with a variety of protein-based radiotracers. . . . . ***Page 1373***

Thakur and colleagues assess the feasibility of ^{64}Cu-TP3982 PET imaging of oncogene VPAC1 receptors overexpressed in human breast cancer cells. . . . . ***Page 1381***

Chen and colleagues use small-animal PET and autoradiographic imaging in prostate cancer–xenografted mice to evaluate ^{64}Cu-radiolabeled gastrin-releasing peptide analogs for imaging peptide receptor expression. . . . . ***Page 1390***

Toyama and colleagues report on the use of ^{18}F-FDG and small-animal PET for investigating the feasibility of absolute quantification of regional cerebral glucose use in a mouse model. . ***Page 1398***

Koort and colleagues describe a laboratory study comparing the ^{18}F-FDG PET characteristics of normal bone healing with those of local osteomyelitis and evaluating the ability of PET to differentiate bone healing from local infection. . . . . ***Page 1406***

Divgi and colleagues determine the maximum tolerated whole-body radiation-absorbed dose for a ^{131}I-labeled fractionated radioimmunotherapy used for metastatic renal cancer. . . . . ***Page 1412***

ON THE COVER

This image depicts localization of ^{64}Cu-DOTA-Lys^{3}-bombesin in PC-3 and CWR22 tumor–bearing mice as determined by microPET imaging (Concorde Microsystems, Inc.) followed by whole-body autoradiography. The microPET image is concordant with the whole-body autoradiographic section. Both the PC-3 tumor and the CWR22 tumor are visible, with clear contrast from the adjacent background. Prominent uptake is also seen in the liver and kidneys, and clearance of activity through the urinary bladder is evident.